Combined thermosolutal buoyancy and surface-tension flows in a cavity

T.-C. Jue

Abstract In this article, the thermosolutal buoyancy and surface-tension convection flows are numerically studied with a fourth-order Runge-Kutta time-splitting finite element method. The physical model for a square cavity containing a top free surface and two different temperature and concentration side walls is described by the Navier-Stokes, energy and species concentration equations. On the track of flow pattern, the existence of surface tension will alter the evolution of the flow field and influence the local heat and mass transfer rates near the top free surface. In addition, the surface tension dominated flow field under a zero-gravity condition is studied for $r = 0$ and 1 to investigate the interaction between thermal surface tension and solutal surface tension. The results show that temperature and concentration make opposing contributions to the flow and display local variance in temperature and concentration distributions near surface boundary.

List of symbols

C	concentration
L	cavity width
Le	Lewis number
$\mathrm{Ma}_c, \mathrm{Ma}_T$	species and thermal Marangoni numbers
N	buoyancy ratio
Nu	Nusselt number
P	dimensionless pressure
Pr	Prandtl number
r	surface tension ratio
$\mathrm{Ra}_c, \mathrm{Ra}_T$	species and thermal Rayleigh numbers
Sh	Sherwood number
T	dimensional temperature
t	dimensional time
u, v	dimensional x, y velocities
$\mathbf{U}$	dimensionless velocity vector
x, y	dimensional Cartesian coordinates
α	thermal diffusivity
β_c, β_T	expansion coefficients for concentration and temperature
γ_c, γ_T	solutal and thermal surface tension gradients
μ	dynamic viscosity
v	kinematic viscosity
θ	dimensionless temperature
ρ	fluid density
σ	fluid surface tension

1
Introduction

It is well known that convection motion can be induced by buoyancy forces in the domain or surface tension force from the boundary with a free surface due to a temperature difference. However, the convection flow can also be driven by the solutally induced density difference in the domain or surface tension variation on the free surface. In fact, many practical flow fields such as material processing and crystal growth are caused by both temperature and concentration effects, and driven by both buoyancy convection and capillary convection simultaneously [1, 2, 3]. Up to date, most of the efforts have been given to the investigation of temperature gradient induced buoyancy convection flow and thermocapillary convection flow [4, 5, 6, 7]. Therefore, the study of the interaction between these two flows and the effects of these two factors will be important and interesting for researchers because of its complex physical phenomena and the nonlinear characteristics among the equations.

In reviewing previous research, a double-diffusive Marangoni convection study was performed by Bergman [8] for steady state results to understand the interaction between thermocapillary flow and diffusocapillary flow. About the flow field in solidification, an analysis of binary solid-liquid phase change with buoyancy and surface tension driven convection was conducted by Incropera et al. [9] with a numerical method for zero-gravity and one-gravity environments. Dong et al. [10] investigated the double diffusive convection in a trapezoidal enclosure with thermocapillary effect in steady state condition, and the study provided a series of results for different Ma_T.

In this research, a thermosolutal surface tension and buoyancy driven convection flow is studied to discover the interactions between surface tension and buoyancy effects, and the fluid flows caused by different ratio of solutal and thermal surface tension forces. The dimensionless parameters contained in the physical model include $\mathrm{Ra}_T, \mathrm{Ma}_T, \mathrm{Ma}_c, \mathrm{Pr}, \mathrm{Le}, N$ and r. It is a formidable task to perform the cases for a wide range of all the parameters. Particularly, the primary purpose is to investigate the interaction between temperature- and concentration-induced surface tension flow and natural convection flow, so the

physical cases considered here are concentrated on different Ra_T, Ma_T, r, and the remaining parameters are kept at the same values.

2
Mathematical model
The physical domain considered is a 2-D square cavity with aspect ratio 1. The physical model involves continuity, momentum, energy and species concentration equations. A Newtonian, incompressible fluid is considered for the laminar flow in the cavity. The density variation of the fluid follows Boussinesq's assumption and changes with temperature as well as concentration. The free surface of liquid is assumed to be perfectly flat corresponding to an approximately zero capillary number free surface [11], and surface tension along the free surface varies linearly with temperature and/or concentration gradients only. Soret, Dufour and viscous dissipation effects are neglected in this model.

The dependence of density and surface tension on temperature and concentration can be expressed as

$$\rho = \rho_0 \left(1 - \beta_T(T - T_0) - \beta_c(c - c_0)\right) \tag{1}$$

$$\sigma = \sigma_0 \left(1 - \gamma_T(T - T_0) - \gamma_c(c - c_0)\right) \tag{2}$$

The subscript 0 refers to reference state. For most of the liquids β_T and γ_T are positive. In this study, $\beta_T, \gamma_T, \gamma_c$ are set positive and β_c is negative. By applying the above assumptions, the nondimensionalized governing equations can be derived as:
Continuity equation:

$$\frac{\partial U}{\partial X} + \frac{\partial V}{\partial Y} = 0 \tag{3}$$

x-momentum equation:

$$\frac{\partial U}{\partial \tau} + U\frac{\partial U}{\partial X} + V\frac{\partial U}{\partial Y} = -\frac{\partial P}{\partial X} + \Pr\left(\frac{\partial^2 U}{\partial X^2} + \frac{\partial^2 U}{\partial Y^2}\right) \tag{4}$$

y-momentum equation:

$$\frac{\partial V}{\partial \tau} + U\frac{\partial V}{\partial X} + V\frac{\partial V}{\partial Y} = -\frac{\partial P}{\partial Y} + \Pr\left(\frac{\partial^2 V}{\partial X^2} + \frac{\partial^2 V}{\partial Y^2}\right)$$
$$+ Ra \cdot \Pr \cdot (\theta + N \cdot C) \tag{5}$$

Energy equation:

$$\frac{\partial \theta}{\partial \tau} + U\frac{\partial \theta}{\partial X} + V\frac{\partial \theta}{\partial Y} = \left(\frac{\partial^2 \theta}{\partial X^2} + \frac{\partial^2 \theta}{\partial Y^2}\right) \tag{6}$$

Species concentration equation:

$$\frac{\partial C}{\partial \tau} + U\frac{\partial C}{\partial X} + V\frac{\partial C}{\partial Y} = \frac{1}{Le}\left(\frac{\partial^2 C}{\partial X^2} + \frac{\partial^2 C}{\partial Y^2}\right) \tag{7}$$

In the above, the nondimensional quantities are defined as

$U = [u/(\alpha/L)], \quad V = [v/(\alpha/L)], \quad X = x/L, \quad Y = y/L,$

$\tau = [t/(L^2/\alpha)], \quad P = p/(\rho\alpha^2/L^2), \quad \theta = (T - T_0)/\Delta T,$

$C = (c - c_0)/\Delta c, \quad T_0 = (T_h + T_l)/2, \quad c_0 = (c_H + c_L)/2,$

$\Pr = \nu/\alpha, \quad Le = \alpha/D, \quad Ra_T = g\beta_T\Delta T L^3/\alpha\nu,$

$Ra_c = g\beta_c\Delta c L^3/\alpha\nu, \quad N = \beta_c\Delta c/\beta_T\Delta T,$

$$Ma_T = \partial\sigma/\partial T|_c \Delta T L/(\mu\alpha), \quad Ma_c = \partial\sigma/\partial c|_T \Delta c L/(\mu\alpha)$$

$$\Delta T = T_h - T_l, \quad \Delta c = c_H - c_L \tag{8}$$

In order to consider the relative contribution of Ma_T and Ma_c easily, a ratio of the two numbers is defined as

$$r = \frac{\partial\sigma/\partial c|_T \Delta c}{\partial\sigma/\partial T|_c \Delta T} \tag{9}$$

The boundary conditions on the fixed surface are specified as (see Fig. 1(a)):

$$U = V = 0, \quad \theta = \theta_h = 0.5, \quad C = C_L = -0.5, \quad (X = 0) \tag{10}$$

$$U = V = 0, \quad \theta = \theta_l = -0.5, \quad C = C_H = 0.5, \quad (X = 1) \tag{11}$$

$$U = 0, \quad V = 0, \quad \frac{\partial\theta}{\partial Y} = 0, \quad \frac{\partial C}{\partial Y} = 0, \quad (Y = 0) \tag{12}$$

while the free-surface boundary conditions are given by:

$$\frac{\partial U}{\partial Y} = Ma_T\frac{\partial\theta}{\partial X} + Ma_c\frac{\partial C}{\partial X},$$

$$V = 0, \quad \frac{\partial\theta}{\partial Y} = 0, \quad \frac{\partial C}{\partial Y} = 0, \quad (Y = 1) \tag{13}$$
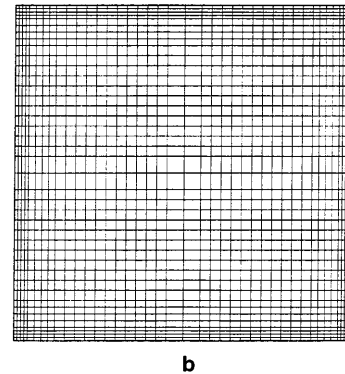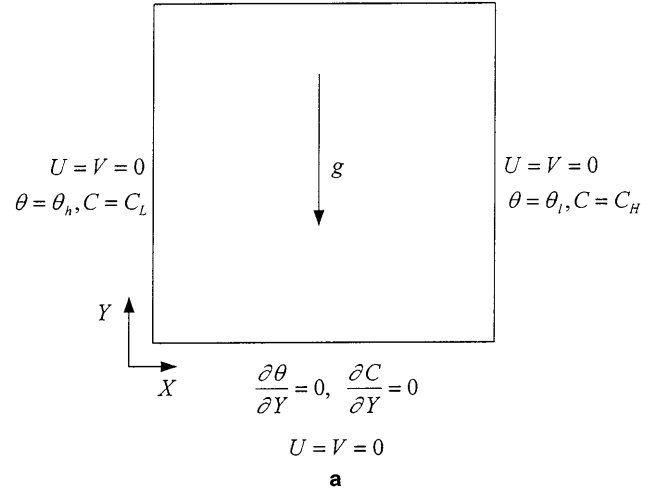

Fig. 1. a Problem definition; b finite element mesh

The shear stress on the left-hand side of Eq. (13) is responsible for the surface tension convection and occurs whenever the surface tension varies with the liquid temperature or concentration.

3
Solution method

The solution procedure consists of a fourth-order Runge-Kutta method for the time dependent governing equations and an explicit Euler scheme to express the convection and diffusion terms. In solving the momentum equations, the time-splitting scheme is applied and the momentum equations are decomposed into an intermediate velocity phase and a corrected velocity phase. The intermediate velocity phase is obtained by solving the momentum equation without including pressure term, while the pressure is acquired from a Poisson equation deriving from the continuity constraint. Finally, the pressure and intermediate velocity are used to find the correct velocity. After solving the momentum equations, the energy and concentration equations are solved by using the correct velocity. The solution procedure can be described as follows:

Step 1:
   Phase 1:

$$\bar{\mathbf{U}}^{n+1(1)} = \mathbf{U}^n + \frac{\Delta\tau}{2}(\mathrm{Pr}\nabla^2\mathbf{U} - \mathbf{U}\cdot\nabla\mathbf{U} + S)^n \tag{14.1}$$

$$\nabla^2 P = 2\frac{\nabla\cdot\bar{\mathbf{U}}^{n+1(1)}}{\Delta\tau} \tag{14.2}$$

$$\mathbf{U}^{n+1(1)} = \bar{\mathbf{U}}^{n+1(1)} - \frac{\Delta\tau}{2}\nabla P \tag{14.3}$$

$$\nabla\cdot\mathbf{U}^{n+1(1)} = 0 \tag{14.4}$$

where S is the source term representing 0 and $\mathrm{Ra}\cdot\mathrm{Pr}(\theta + N\cdot C)$ in x and y momentum equations, respectively.
   Phase 2:

$$\bar{\mathbf{U}}^{n+1(2)} = \mathbf{U}^n + \frac{\Delta\tau}{2}(\mathrm{Pr}\nabla^2\mathbf{U} - \mathbf{U}\cdot\nabla\mathbf{U} + S)^{n+1(1)} \tag{15.1}$$

$$\nabla^2 P = 2\frac{\nabla\cdot\bar{\mathbf{U}}^{n+1(2)}}{\Delta\tau} \tag{15.2}$$

$$\mathbf{U}^{n+1(2)} = \bar{\mathbf{U}}^{n+1(2)} - \frac{\Delta\tau}{2}\nabla P \tag{15.3}$$

$$\nabla\cdot\mathbf{U}^{n+1(2)} = 0 \tag{15.4}$$

   Phase 3:

$$\bar{\mathbf{U}}^{n+1(3)} = \mathbf{U}^n + \frac{\Delta\tau}{2}(\mathrm{Pr}\nabla^2\mathbf{U} - \mathbf{U}\cdot\nabla\mathbf{U} + S)^{n+1(2)} \tag{16.1}$$

$$\nabla^2 P = 2\frac{\nabla\cdot\bar{\mathbf{U}}^{n+1(3)}}{\Delta\tau} \tag{16.2}$$

$$\mathbf{U}^{n+1(3)} = \bar{\mathbf{U}}^{n+1(3)} - \frac{\Delta\tau}{2}\nabla P \tag{16.3}$$

$$\nabla\cdot\mathbf{U}^{n+1(3)} = 0 \tag{16.4}$$

   Phase 4:

$$\bar{\mathbf{U}}^{n+1(4)} = \mathbf{U}^n + \Delta\tau\left(\frac{F(\mathbf{U})^n}{6} + \frac{F(\mathbf{U})^{n+1(1)}}{3}\right.$$
$$\left. + \frac{F(\mathbf{U})^{n+1(2)}}{3} + \frac{F(\mathbf{U})^{n+1(3)}}{6}\right) \tag{17.1}$$

$$\nabla^2 P = \frac{\nabla\cdot\bar{\mathbf{U}}^{n+1(4)}}{\Delta\tau} \tag{17.2}$$

$$\mathbf{U}^{n+1} = \bar{\mathbf{U}}^{n+1(4)} - \Delta\tau\nabla P \tag{17.3}$$

$$\nabla\cdot\mathbf{U}^{n+1} = 0 \tag{17.4}$$

where $F(\mathbf{U}) = \mathrm{Pr}\nabla^2\mathbf{U} - \mathbf{U}\cdot\nabla\mathbf{U} + S$.

Step 2:
   Phase 1:

$$\theta^{n+1(1)} = \theta^n + \frac{\Delta\tau}{2}(\nabla^2\theta^n - \mathbf{U}^{n+1}\cdot\nabla\theta^n) \tag{18}$$

   Phase 2:

$$\theta^{n+1(2)} = \theta^n + \frac{\Delta\tau}{2}(\nabla^2\theta^{n+1(1)} - \mathbf{U}^{n+1}\cdot\nabla\theta^{n+1(1)}) \tag{19}$$

   Phase 3:

$$\theta^{n+1(3)} = \theta^n + \frac{\Delta\tau}{2}(\nabla^2\theta^{n+1(2)} - \mathbf{U}^{n+1}\cdot\nabla\theta^{n+1(2)}) \tag{20}$$

   Phase 4:

$$\theta^{n+1} = \theta^n + \Delta\tau[1/6(\nabla^2\theta^n - \mathbf{U}^{n+1}\cdot\nabla\theta^n)$$
$$+1/3(\nabla^2\theta^{n+1(1)} - \mathbf{U}^{n+1}\cdot\nabla\theta^{n+1(1)})$$
$$+1/3(\nabla^2\theta^{n+1(2)} - \mathbf{U}^{n+1}\cdot\nabla\theta^{n+1(2)})$$
$$+1/6(\nabla^2\theta^{n+1(3)} - \mathbf{U}^{n+1}\cdot\nabla\theta^{n+1(3)})] \tag{21}$$

Step 3:
   Phase 1:

$$C^{n+1(1)} = C^n + \frac{\Delta\tau}{2}\left(\frac{1}{\mathrm{Le}}\nabla^2 C^n - \mathbf{U}^{n+1}\cdot\nabla C^n\right) \tag{22}$$

   Phase 2:

$$C^{n+1(2)} = C^n + \frac{\Delta\tau}{2}\left(\frac{1}{\mathrm{Le}}\nabla^2 C^{n+1(1)} - \mathbf{U}^{n+1}\cdot\nabla C^{n+1(1)}\right) \tag{23}$$

   Phase 3:

$$C^{n+1(3)} = C^n + \frac{\Delta\tau}{2}\left(\frac{1}{\mathrm{Le}}\nabla^2 C^{n+1(2)} - \mathbf{U}^{n+1}\cdot\nabla C^{n+1(2)}\right) \tag{24}$$

Phase 4:

$$
\begin{aligned}
C^{n+1} = C^n + \Delta\tau \Bigg[& 1/6\left(\frac{1}{\text{Le}}\nabla^2 C^n - \mathbf{U}^{n+1}\cdot\nabla C^n\right) \\
& +1/3\left(\frac{1}{\text{Le}}\nabla^2 C^{n+1(1)} - \mathbf{U}^{n+1}\cdot\nabla C^{n+1(1)}\right) \\
& +1/3\left(\frac{1}{\text{Le}}\nabla^2 C^{n+1(2)} - \mathbf{U}^{n+1}\cdot\nabla C^{n+1(2)}\right) \\
& +1/6\left(\frac{1}{\text{Le}}\nabla^2 C^{n+1(3)} - \mathbf{U}^{n+1}\cdot\nabla C^{n+1(3)}\right) \Bigg]
\end{aligned}
$$

$$(25)$$

Following the above procedures, a Galerkin finite element method with 4-node isoparametric element is applied to solve the above equations. The advantages of this numerical methodology are that the variables can be solved separately to reduce the size of stiffness matrices by using time-splitting scheme, and the time step used can be much larger than that of the first-order projection scheme. Because of these benefits, the problem is solved in an accurate and economic procedure. A detailed description and complete results for the benchmark problems such as standing vortex problem, driven cavity flow, and flow past a square cylinder are available in the paper of Ling et al. [12].

4
Results and discussion

The results shown in this section are calculated from zero initial velocities and mean values of temperature and concentration. A grid independence study is carried out for a thermally driven cavity flow at $Pr = 0.71$, $Ra = 10^6$ with 21×21, 31×31, 41×41 and 51×51 meshes, and the flow quantities are listed in Table 1. Because of the computational cost and accuracy considerations (Table 1, 2), a 41×41 mesh (Fig. 1b) is used for the following study. The

Table 1. Comparison with benchmark solutions for the case $Pr = 0.71$, $Ra = 10^6$

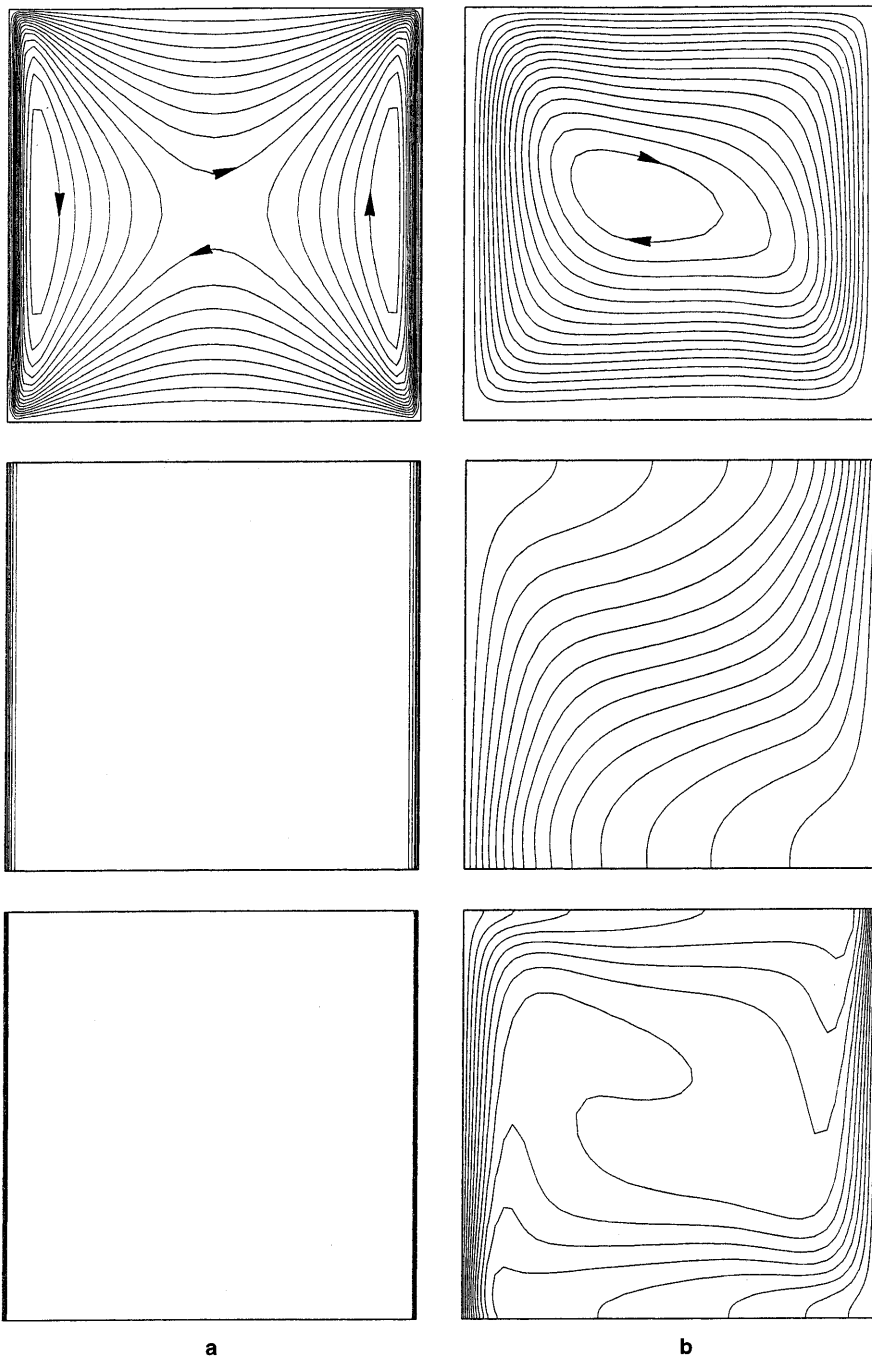| Meshes and benchmark solutions	$\|\Psi_{\text{mid}}\|$	$\|\Psi_{\text{max}}\|$	u_{max}	v_{max}
21×21	16.02	16.87	63.92	245.46
31×31	16.23	16.75	63.63	233.27
41×41	16.30	16.82	64.61	217.62
51×51	16.35	16.81	64.48	226.11
De Vahl Davis [13] (80 by 80 uniformed mesh)	16.32	16.75	64.63	219.36

steady state results are calculated by following the criterion for convergence

$$\frac{\|\Phi^{n+1} - \Phi^n\|_1}{\|\Phi^n\|_1} \le 1.0 \times 10^{-4} \tag{26}$$

where Φ refers to U, V, θ and C. $\|\Phi\|_1$ is the L_1 norm obtaining as the sum of the absolute value of the variable components on the interior grid multiplied by the cell size.

Figure 2 illustrates the streamlines, isotherms and iso-concentration lines for $Ra_T = 10^4$, $Pr = 7.6$, $Le = 10$, $N = -5$, and $Ma_T = Ma_c = 0$ at $\tau = 10^{-4}$ and steady state. At small time $\tau = 10^{-4}$, both the thermal and solutal buoyancy forces excite the fluid near the left hot, low concentration wall to flow up and the fluid near the right cold, high concentration wall to flow down resulting in the cellular flow pattern with a primary clockwise cell including two secondary cells in it. The contours of temperature and concentration distributions are located near and parallel with the vertical walls due to the diffusion-dominant heat and mass transfer in the low velocity flow at this time. As the time increases, the strength of the main cell gradually raises and the two secondary cells move close to merge together. Finally, only the primary cell exists in the domain for steady state results, and the isotherms and isoconcentration lines display a convection-dominant pattern where the isoconcentration lines are distorted more seriously than the isotherms.

To compare with $Ma_T = Ma_c = 0$ results, the following cases are studied for $Ma_T = 10^2$, -10^2 and $r = 0$, and the remaining parameters are kept the same. The $r = 0$ means $Ma_c = 0$ for simplifying the condition to easily compare with the without surface tension case. In $Ma_T = 10^2$ condition, the surface tension forces the fluid on the top surface to flow in the left direction, and form two small counterclockwise cells at two top corners at $\tau = 10^{-4}$ (Fig. 3a). Because the direction of surface tension flow is opposite to the buoyancy flow, this phenomenon corresponds to an opposing condition. However, the isotherms and isohalines are similar to those in Fig. 2a still in diffusion-dominant status. Due to the strength of surface tension flow much smaller than that of buoyancy flow in this case, the surface-tension driven cells finally disappear in the domain and the contours of stream lines, temperature and concentration distributions are almost the same as without surface tension effect results (Fig. 2b) and not to be displayed repeatedly. On the other hand, the $Ma_T = -10^2$ condition creates two clockwise small cells at two top corners and are involved in the two buoyancy driven secondary cells (Fig. 3b). This status corresponds to an augmenting case for the surface-tension flow and the buoyancy flow are in the same direction now. The primary cell and secondary cells gradually merge together and the

Table 2. Comparison of results computed by 41×41 mesh with benchmark solutions (listed in bracket) [13]

Ra	$\|\Psi_{\text{mid}}\|$	$\|\Psi_{\text{max}}\|$	u_{max}	v_{max}
10^3	1.174 (1.174)	1.174	3.643 (3.649)	3.706 (3.697)
10^4	5.083 (5.071)	5.083	16.239 (16.178)	19.722 (19.617)
10^5	9.174 (9.111)	9.700 (9.612)	35.314 (34.73)	69.057 (68.59)
10^6	16.30 (16.32)	16.82 (16.750)	64.61 (64.63)	217.62 (219.36)

Fig. 2a, b. Streamlines, isotherms and isoconcentration lines (from top to bottom) for $Ra_T = 10^4$, $Pr = 7.6$, $Le = 10$, $N = -5$, $Ma_T = Ma_c = 0$. **a** $\tau = 10^{-4}$; **b** steady state

final steady state results are still almost the same as without surface tension results (Fig. 2b).

In addition to $Ma_T = 10^2$ and -10^2, a larger Ma_T value is also interested in this research. The results for $Ma_T = 10^3$, -10^3 and $r = 0$ are studied and displayed in Fig. 4a, b. For $Ma_T = 10^3$, $r = 0$, the streamlines, isotherms and isohalines are presented in Fig. 4a and it is easily to find the effect of thermal surface tension existing in the upper area of the domain for a counterclockwise cell created by surface tension appearing in this area, besides the main clockwise cell driven by buoyancy force. Because the circulation induced by surface tension is strong now, the flow field is dominated by both forces simultaneously.

About the temperature distribution, the contours in the lower area are affected by natural convection to curve in right direction and those in the upper portion are dominated by surface tension flow to be distorted in left direction. In particular, the isoconcentration distribution shows a seriously distorted and complicated distribution. On the other hand, the streamlines for $Ma_T = -10^3$ present an augmenting phenomenon with much stronger circulation comparing with those of $Ma_T = -10^2$. There are sharp turning flows appearing at top right corner and the center of primary cell moves upper than $Ma_T = -10^2$ results. The flow phenomena result in the isotherms with a strong convection affected distribution showing a large
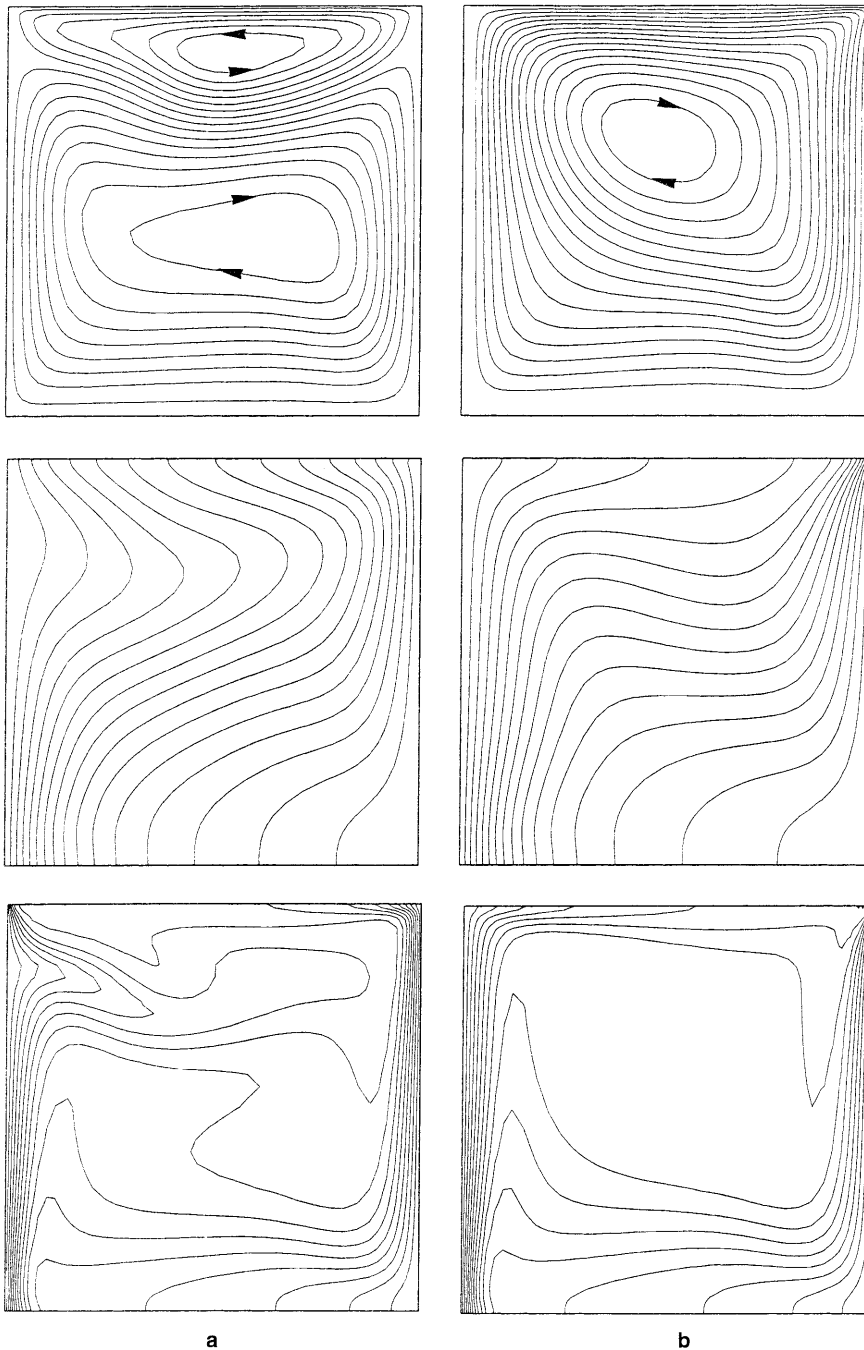
a

b
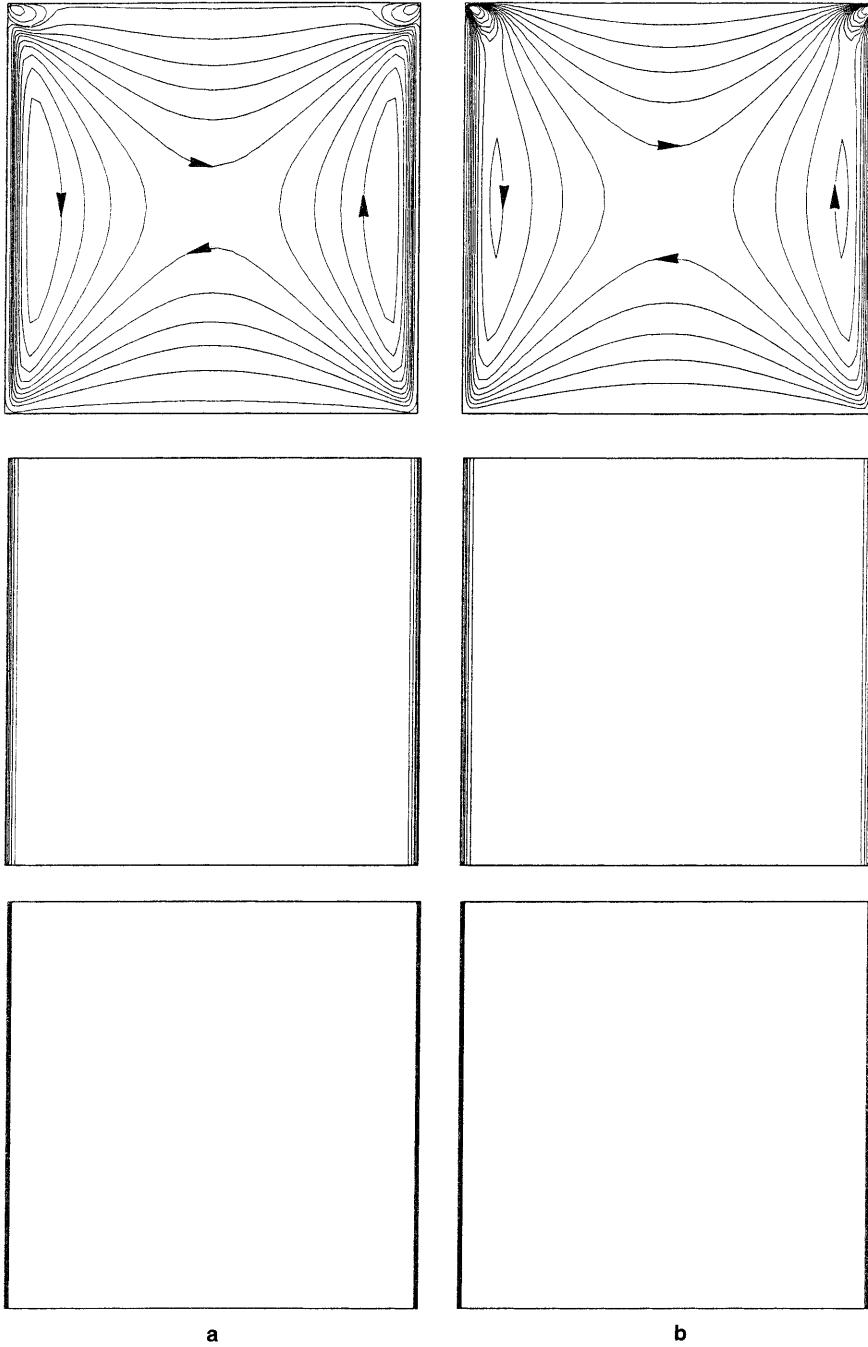
Fig. 3a, b. Streamlines, isotherms and isoconcentration lines (from top to bottom) for $Ra_T = 10^4$, $Pr = 7.6$, $Le = 10$, $N = -5$, $r = 0$, $\tau = 10^{-4}$. **a** $Ma_T = 10^2$; **b** $Ma_T = -10^2$

temperature gradient around top right corner. Similarly, the isoconcentration distributions display a much curved pattern in central area because of the influence of convection flow field.

In many practical systems, convective conditions within the bulk fluid govern the local heat and mass transfer rates, and result in the local transfer rates varying significantly. Therefore, the local Nusselt number and Sherwood number are shown in Fig. 5a, b to display a measure of the local dimensionless heat and mass transfer rates. The Nu and Sh are defined as

$$\text{Nu} = \left|\frac{\partial \theta}{\partial x}\right|, \quad \text{Sh} = \left|\frac{\partial C}{\partial x}\right|. \quad (27)$$

On the left wall, the values of Nusselt number and Sherwood number show a local maximum near the bottom area due to the local turning of flow direction, and then decrease to a minimum value at the top surface point, except the values for $Ma_T = 10^3$, $r = 0$ (Fig. 5a). The distributions for without surface tension effect and with surface tension effect for $Ma_T = 10^2$, -10^2, $r = 0$ are almost the same, because the flow field is dominated by buoyancy convection flow. The Nu and Sh of $Ma_T = -10^3$, $r = 0$ case are greater than the above three conditions, due to the augmenting influence. For $Ma_T = 10^3$, $r = 0$, the counteracting effect between buoyancy flow and surface tension flow results in existing a turning point around $y = 0.79$ for Nu distribution and $y = 0.85$ for Sh distribution, and then

Fig. 4a, b. Steady state streamlines, isotherms and isoconcentration lines (from top to bottom) for $Ra_T = 10^4$, $Pr = 7.6$, $Le = 10$, $N = -5$, $r = 0$. **a** $Ma_T = 10^3$; **b** $Ma_T = -10^3$

increasing to a maximum value. On the other hand, the Nu and Sh distributions on the right wall first increase from bottom to near the top area, and divided to two groups (Fig. 5b). One for augmenting status presents bigger values than those of without surface condition and increases to a maximum value on the top surface; the other for counteracting status displays smaller values than without surface results.

In addition to without solutal surface tension effect $r = 0$, the following conditions are concentrated on the effect of solutal Marangoni flow by increasing the value of r. The conditions are set as $Ma_T = -10^3$, $r = 0.2, \ 0.4, \ 0.8$ and 1 corresponding to $Ma_c = -2 \times 10^2$, -4×10^2, -8×10^2 and -10^3, respectively. The streamlines, isotherms and isohalines for $Ma_T = -10^3$, $r = 0.2$, 0.4 are very similar to the results of $Ma_T = -10^3$, $r = 0$ and the difference among the three cases is the strength of circulation, which is stronger for the smaller value of r due to the direction of solutal Marangoni flow opposite to the thermal Marangoni flow. However, the streamlines of $Ma_T = -10^3$, $r = 0.8$, 1 (Fig. 6) display some differences from the above two cases that the flow field includes two small counterclockwise cells in top corner area and the center of circulation moves a little to left and lower for the opposing solutal surface tension effect, but the isotherms and isohalines are still very similar. About the local heat
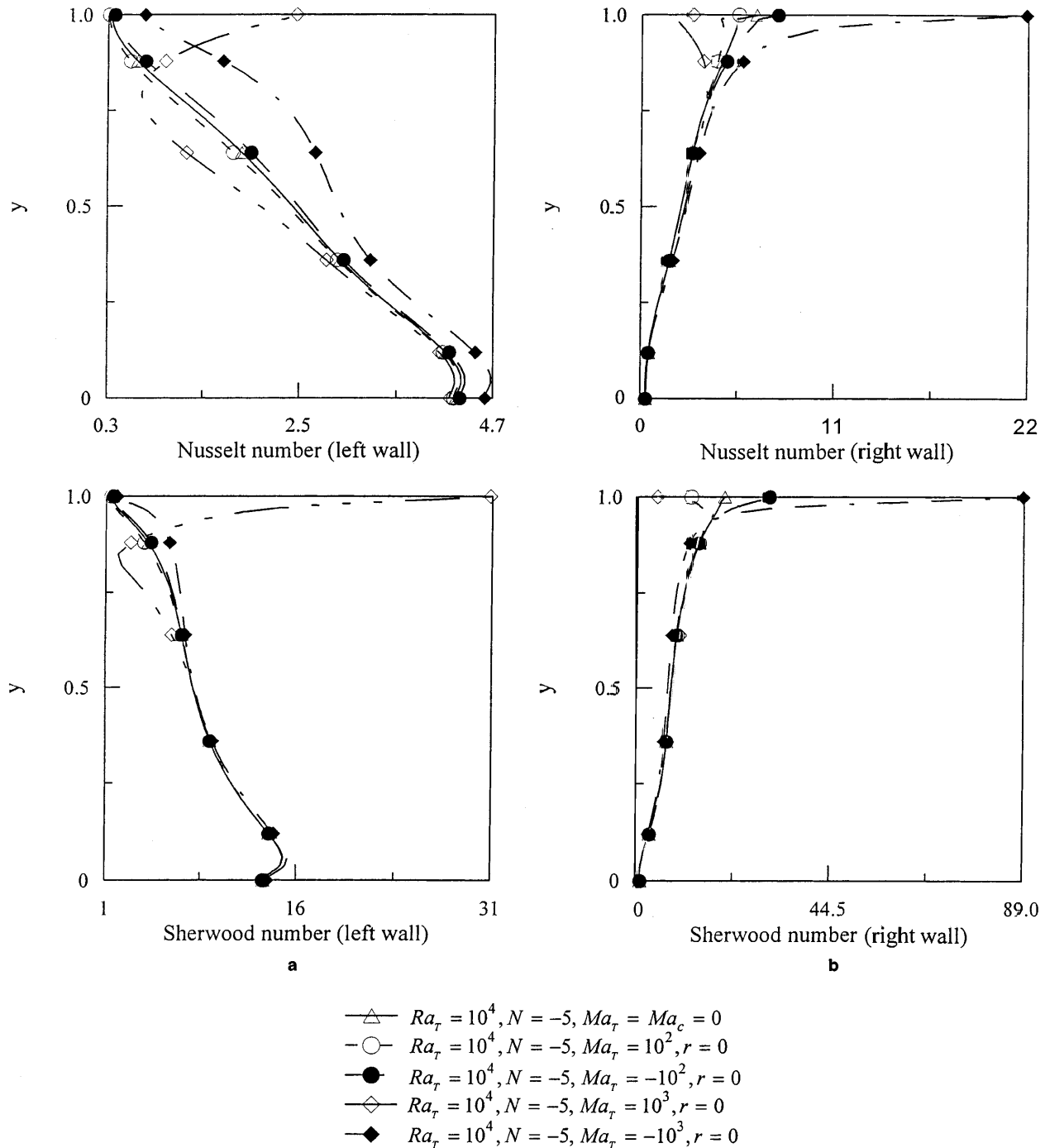
Fig. 5a, b. Local Nusselt number and Sherwood number. **a** Left wall; **b** right wall

and mass transfer rates on both side walls, the patterns are basically the same because the flow fields are similar for these cases. Smaller r value presents bigger maximum local value on the top surface for less opposing solutal surface tension influence and the values for $r = 0.8$ and 1 display a turning point near the top surface because of the two solutally driven cells existing in this area (Fig. 7).

Besides the normal gravity condition, low gravity condition is an important environment for material researchers to find a new production process. In low gravity environment, the surface tension convection dominates the whole domain; therefore the zero-g gravity condition is an important condition for researchers to study. In the following conditions, the $Ra_T = Ra_c = 0$ corresponds to the zero gravity condition and Ma_T is set as -10^2 and -10^3. Surface tension ratio r is assigned as 0 for pure thermo-surface-tension existing only and 1 for thermo-surface-tension as well as solutal-surface-tension existing simultaneously. The flow pattern presents a single clockwise cell in the domain as shown in Fig. 8a for
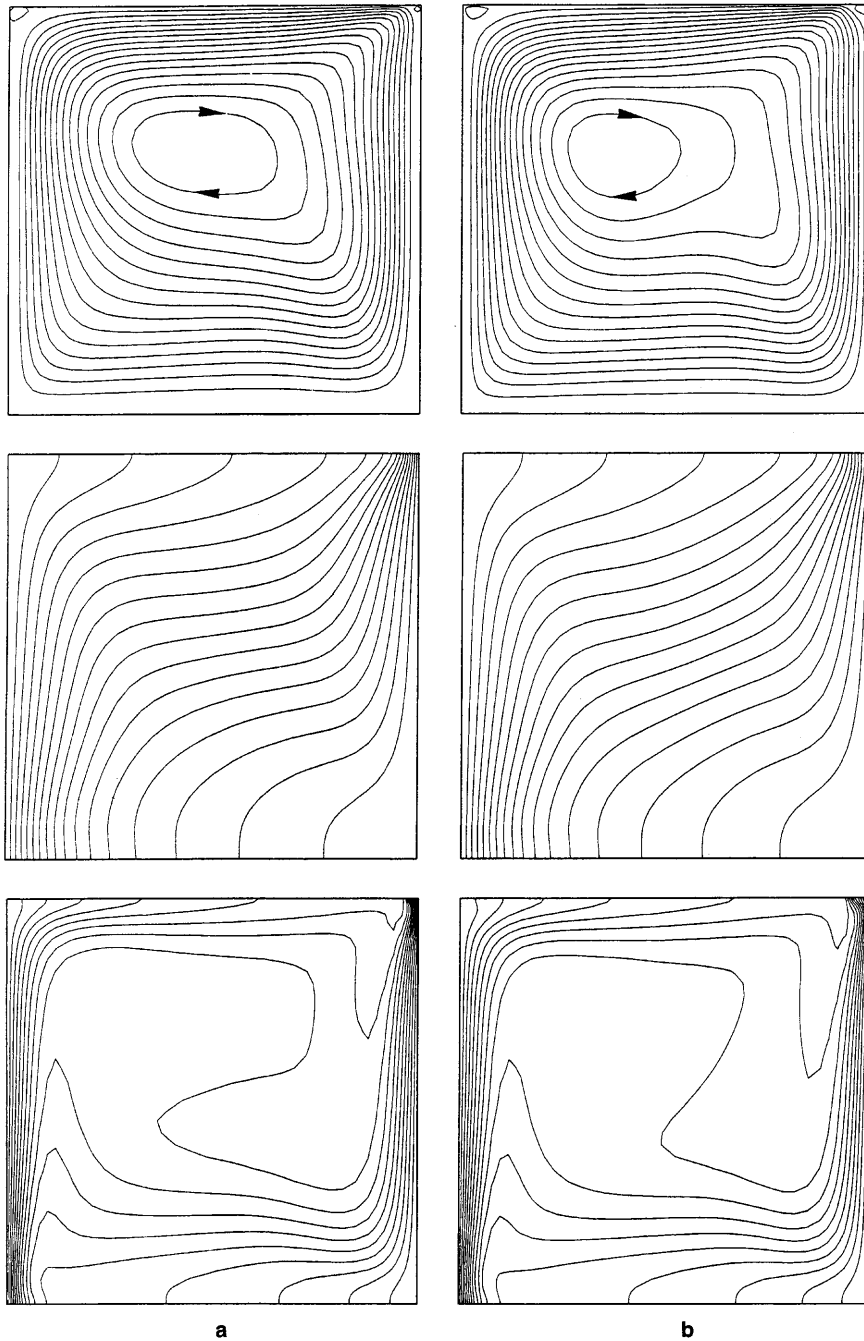
Fig. 6a, b. Steady state streamlines, isotherms and isoconcentration lines (from top to bottom) for $Ra_T = 10^4$, $Pr = 7.6$, $Le = 10$, $N = -5$, $Ma_T = -10^3$. **a** $r = 0.8$; **b** $r = 1$

$Ma_T = -10^3$, $r = 0$. Due to the thermo-surface-tension effect existing only, the center of the circulation is located upper than those of including buoyancy conditions and the flow pattern is similar to a lid-driven cavity flow with thermo-surface-tension as the flow driving force. Under the single driving force condition, the isotherms are distorted mainly in the top portion and the bottom area presents a diffusion type distribution. Similarly, the convection-dominant isohalines exists in the top portion also, but the contours are distorted more seriously than the isotherms in this area. About $Ma_T = -10^3$, $r = 0$ condition, the existing driving forces include thermal surface tension and solutal surface tension, and these two forces

are in opposite direction resulting in a counteracting effect. The streamlines of this condition (Fig. 8b) similar to $Ma_T = -10^3$, $r = 1$ shown in Fig. 6b include two counterclockwise cells created by solutal surface tension effect at two top corners, and this counteracting influence forces the primary circulation driven by thermal surface tension effect to shrink and shift to right. The same influence results in the isotherms and isohalines not curved as much as those of $r = 0$ condition, and additionally the distributions in two top corner areas show opposite direction pattern caused by the two counterclockwise cells. The contours for $Ma_T = -10^2$, $r = 0, 1$ similar to those of $Ma_T = -10^3$, with smaller strength of circulation and little
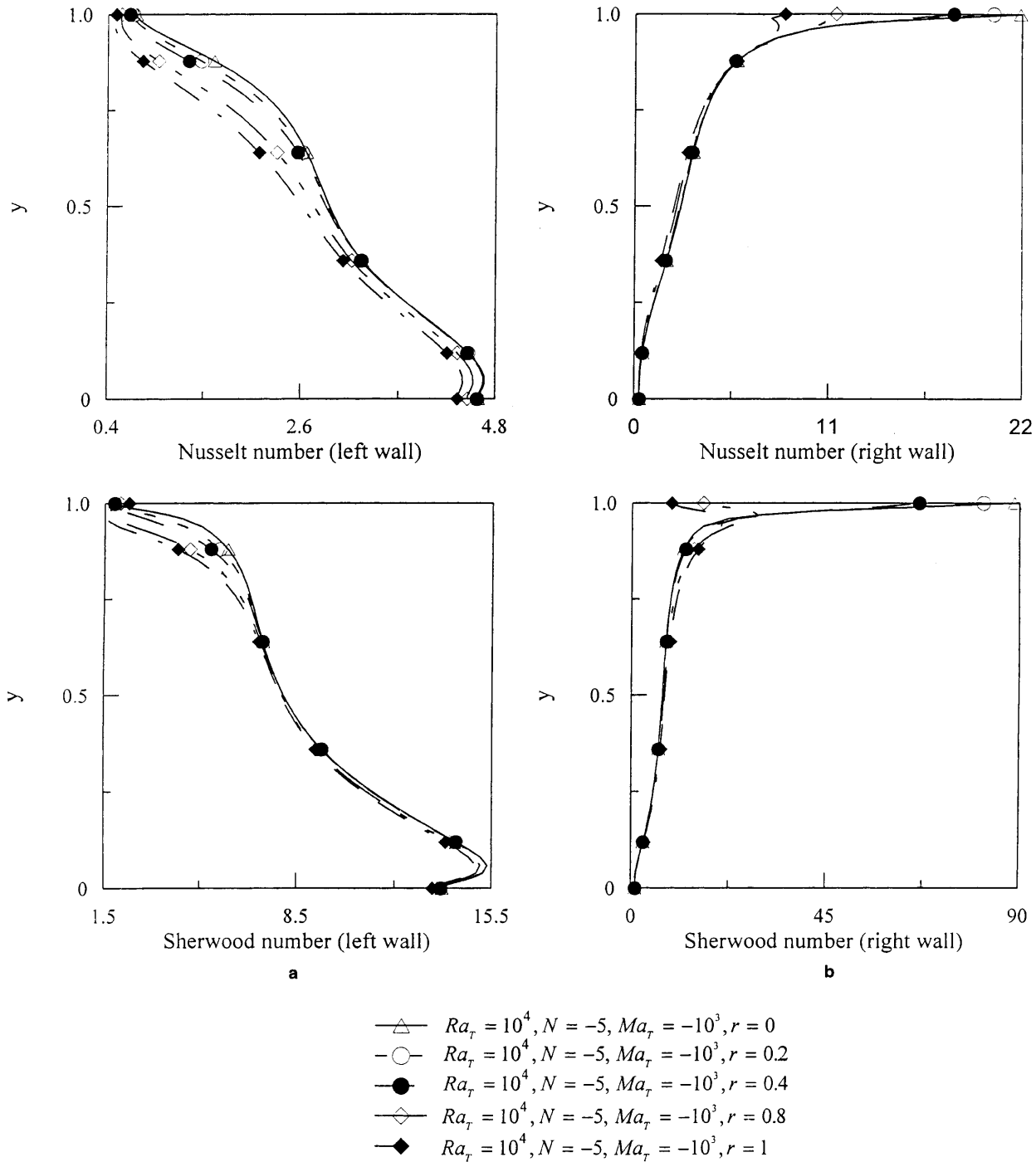
Fig. 7a, b. Local Nusselt number and Sherwood number. **a** Left wall; **b** right wall

distortion of isotherms and isohalines, are not displayed repeatedly. The local heat transfer rate on the left wall is increased with the raise of Ma_T for $r = 0$, and in most area for $r = 1$ except near the top surface resulting from the solutally driven flow effect. The distributions of mass transfer rate are similar for $y < 0.73$, and the lines for $r = 1$ present larger curved pattern after $y = 0.73$ because of the solutal surface tension flow influence also. On the right wall, the same solutal effect causes the lines to bifurcate in the top area; for $r = 0$, the rates approach a maximum value but the values for $r = 1$ decrease.

5
Conclusions
In this paper, a fourth-order Runge-Kutta splitting type finite element method is successfully applied in solving the
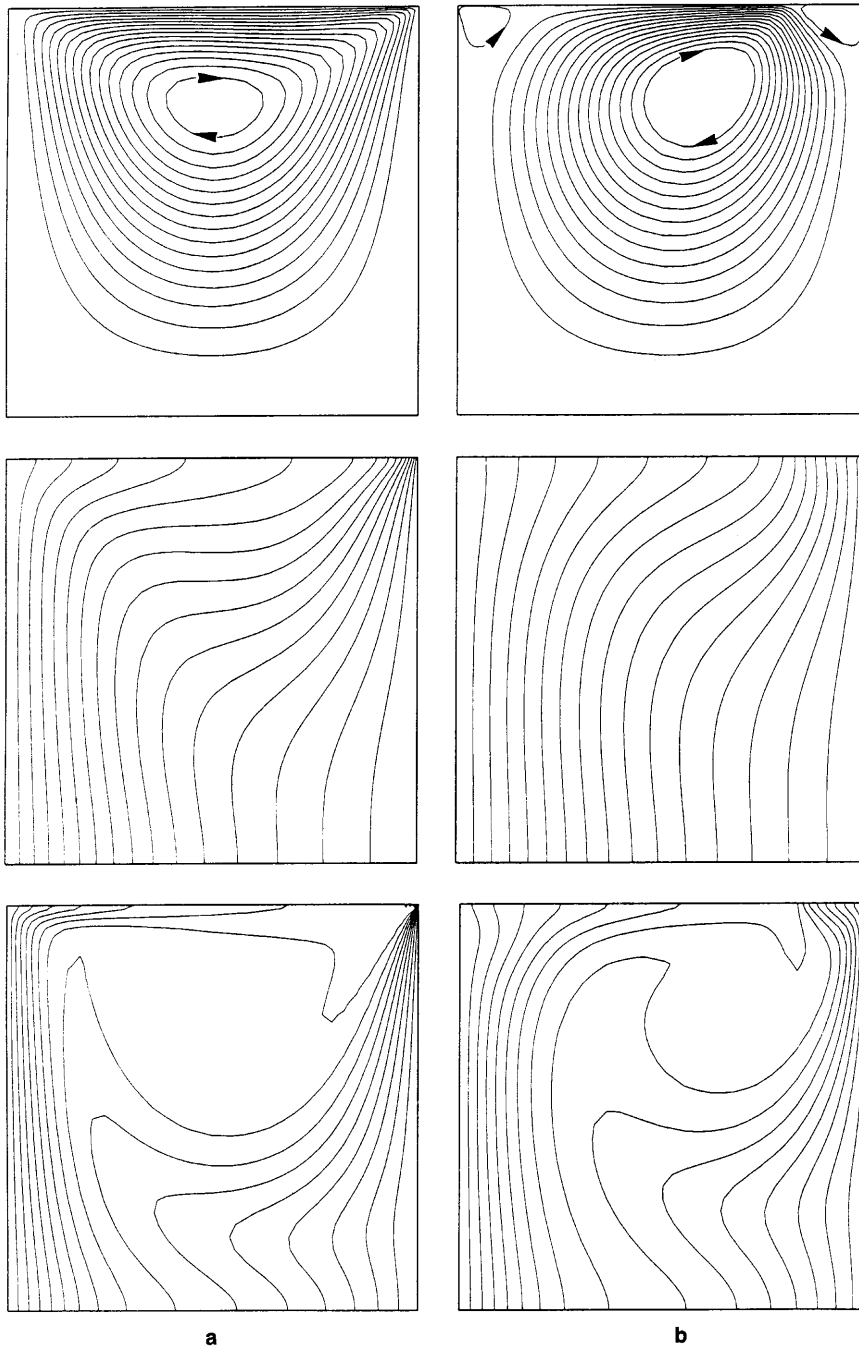
Fig. 8a, b. Steady state streamlines, isotherms and isoconcentration lines (from top to bottom) for $Ra_T = Ra_c = 0$, $Pr = 7.6$, $Le = 10$, $Ma_T = -10^3$. **a** $r = 0$; **b** $r = 1$

thermosolutal convection flow under surface tension effect and buoyancy effect. From this investigation, the surface tension induced flow changes the flow evolution and influence the heat and mass transfer rates near the area of free surface locally. The effects are divided into two kinds. One is the augmenting case for boundary surface tension convection to strengthen domain buoyancy circulation and increase heat and mass transfer rate, close the free surface, and the other is for surface tension flow contrary to the buoyancy convection corresponding to the opposing condition. On the other hand, the solutal surface tension and thermal surface tension are opposing in this study, so the increase of the ratio of solutal surface tension results in reducing the strength of surface tension flow and there are two other cells driven by solutal surface tension for $r \geq 0.8$, $Ma_T = -10^3$. About the zero-gravity condition, the thermal Marangoni convection dominates the whole domain for $r = 0$ status and most area for $r = 1$. However, for $r = 1$ condition, the solutal surface tension creates opposing direction cells to locally affect the heat and mass transfer phenomena and this influence is needed to be noticed in practical applications.
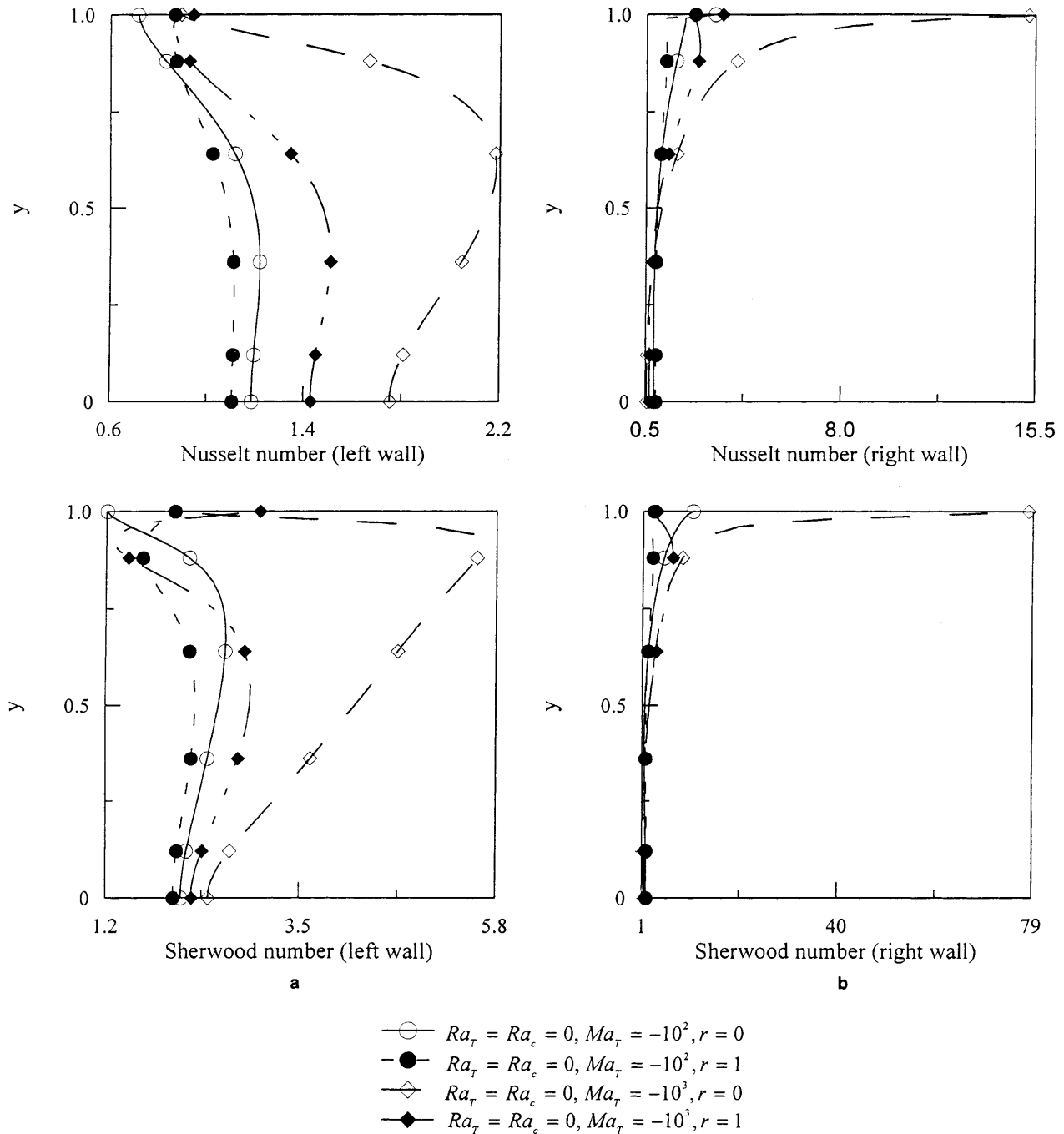
$$\multimap\!\!\circ\quad Ra_T = Ra_c = 0, Ma_T = -10^2, r = 0$$
$$\multimap\!\!\bullet\quad Ra_T = Ra_c = 0, Ma_T = -10^2, r = 1$$
$$\multimap\!\!\diamond\quad Ra_T = Ra_c = 0, Ma_T = -10^3, r = 0$$
$$\multimap\!\!\blacklozenge\quad Ra_T = Ra_c = 0, Ma_T = -10^3, r = 1$$

Fig. 9a, b. Local Nusselt number and Sherwood number.
a Left wall; **b** right wall

References

1. **Pimputkar SM; Ostrach S** (1981) Convection effects in crystals grown from melt. J Crystal Growth 55: 614–646
2. **Ostrach S** (1982) Low-gravity fluid flows. Ann Rev Fluid Mech 14: 313–345
3. **Ostrach S** (1983) Fluid mechanics in crystal growth-The 1982 Freeman Scholar Lecture. J Fluids Eng 105: 5–20
4. **Bergman TL; Keller JR** (1988) Combined buoyancy, surface tension flow in liquid metals. Num Heat Transfer 13: 49–63
5. **Carpenter BM; Homsy GM** (1989) Combined buoyant-thermocapillary flow in a cavity. J Fluid Mech 207: 121–132
6. **Bergman TL; Webb BW** (1990) Simulation of pure metal melting with buoyancy and surface tension forces in liquid phase. Int J Heat Mass Transfer 33: 129–149
7. **Lacroix M** (1991) Effects of buoyancy and surface tension forces on the melting of a metal. Num Heat Transfer Part A 19: 101–115
8. **Bergman TL** (1986) Numerical simulation of double-diffusive Marangoni convection. Phys Fluids 29: 2103–2108
9. **Incropera P; Engel AHH; Bennon WD** (1989) Numerical analysis of binary solid-liquid phase change with buoyancy and surface tension driven convection. Num Heat Transfer Part A 16: 407–427
10. **Dong F; Ebadian MA; Munroe N** (1993) The effect of surface tension on double diffusive convection in a trapezoidal enclosure. Fundamental of Natural Convection, ASME HTD 264: 9–15

11. **Homsy GM; Meiburg E** (1984) The effect of surface contamination on thermocapillary flow in a two-dimensional slot. J Fluid Mech 139: 443–459
12. **Ling LM; Ramaswamy B; Cohen RD; Jue TC** (1993) Numerical analysis on Strouhal frequencies in vortex shedding over square cylinders with surface suction and blowing. Int J Num Heat Fluid Flow 3: 357–375
13. **de Vahl Davis G** (1983) Natural convection of air in a square cavity: a bench mark numerical solution. Int J Num Meth Fluids 3: 249–264